Oxide Electrocatalysts Based on Earth-Abundant Metals for Both Hydrogen- and Oxygen-Evolution Reactions

Ram Krishna Hona[a], Surendra B. Karki[a], Farshid Ramezanipour[a,*]

[a]Department of Chemistry, University of Louisville, Louisville, Kentucky 40292, USA

*Corresponding author. Email: farshid.ramezanipour@louisville.edu, Phone: (502) 852-7061, ORCID: 0000-0003-4176-1386

ABSTRACT

A unique bifunctional oxide electrocatalyst capable of catalyzing both half reactions of water splitting, namely oxygen-evolution reaction (OER) and hydrogen-evolution reaction (HER), with added capability of catalyzing HER in both acidic and basic media, a rare property in water-splitting catalysts, is reported. In addition to bifunctional electrocatalytic properties, $CaSrFeMnO_{6-\delta}$ shows OER activity which is even superior to the reported activities of precious metal electrocatalysts, IrO_2 and RuO_2. The correlation of electrocatalysis with charge-transport properties in the series, $Ca_2FeMnO_{6-\delta}$, $CaSrFeMnO_{6-\delta}$ and $Sr_2FeMnO_{6-\delta}$, is demonstrated. Given the dependence of charge-transport on structure and defects, this work unravels the interesting correlations between the triangle of structure, charge-transport and electrocatalytic activity for water splitting.

Keywords: Electrocatalyst, Earth-abundant, Bifunctional, Water-splitting, Oxide

INTRODUCTION

To achieve efficient water-splitting reaction, it is essential to lower the activation energies of the two half-reactions involved in this process, namely hydrogen-evolution and oxygen-evolution. The oxygen-evolution reaction (OER) in particular has a high activation energy, which leads to considerable overpotential in electrochemical water splitting.

To facilitate the OER process, precious metal catalysts, such as IrO_2,[1] RuO_2,[2] and Ir alloys[3] have been utilized. However, given the high cost of these catalysts, there have been efforts to find more economical alternatives. Among different classes of materials that have been investigated for this purpose, transition metal oxides have shown great promise. In particular, studies on oxygen-deficient perovskites have demonstrated notable electrocatalytic properties.[4-6] Some oxygen-deficient perovskites, such as the well-known $Ba_{0.5}Sr_{0.5}Co_{0.8}Fe_{0.2}O_{3-\delta}$ (BSCF),[7] have shown OER activity close to that of precious metal catalysts,[7] and are considered promising candidates to replace the current high-cost catalysts.

For hydrogen evolution reaction (HER), the high cost of platinum used in Pt/C catalyst[8-10] and some of the Ir-based alternatives[11] has led to the investigation of various other catalysts such as sulphides,[12] phosphides,[13] carbides,[9] and nitrides.[9] However oxides, particularly perovskite oxides, with good HER activity in either acidic[14] or basic[15] condition are not very common. Recently, a perovskite oxide was studied as HER catalyst in alkaline environment.[8] Importantly, perovskite oxides based on non-precious metals that show high HER activity in acidic environment are extremely rare.

Given our prior experience with electrocatalytic properties of oxygen-deficient perovskites,[6] we set out to explore the possibility of finding electrocatalysts based on this family of materials that are capable of catalyzing both half reactions of water splitting. Given the diverse range of structures that are found in this class of oxides,[16-17] it is expected that structural properties can play an important role in directing their catalytic activity. The structure of these materials is a function of the degree of oxygen-deficiency and the arrangement of vacant sites

within the crystal lattice. The vacancies can be distributed randomly in the structure, or show different types of ordering. There is a variety of vacancy-ordered structures including those containing different combinations of square-pyramidal, tetrahedral or octahedral geometries.[16-17]

The electrocatalytic materials studied in this work, $Ca_2FeMnO_{6-\delta}$, $CaSrFeMnO_{6-\delta}$ and $Sr_2FeMnO_{6-\delta}$, belong to the oxygen-deficient perovskite family, and their magnetic properties have been studied previously.[18-19] This series show an interesting trend in the distribution of oxygen-vacancies and structural order. In this article, we demonstrate that these materials are outstanding electrocatalysts for water-splitting and show unique bifunctional properties. We also show the correlations between crystal structure and electrocatalytic activity for both hydrogen- and oxygen-evolution reaction. Furthermore, we demonstrate the relationship between structural properties and electrical charge-transport, which in turn affects the electrocatalytic properties of these materials. The significance of these catalysts is not due to a single characteristic, but is a result of a combination of properties. While each individual feature may be found in some other materials, the combination of all these properties in the same compound makes the reported catalysts particularly remarkable. Those properties include high electrocatalytic activity for both half-reactions of water splitting, OER and HER, the use earth abundant elements instead of precious metals, the ability to catalyze HER in both acidic and basic media, superior OER activity to the reported precious-metal oxide catalysts, and intrinsic bifunctional electrocatalytic activity as single-phase bulk material, without the need for nanofabrication or composite formation.

EXPERIMENTAL

The materials $Ca_2FeMnO_{6-\delta}$, $CaSrFeMnO_{6-\delta}$ and $Sr_2FeMnO_{6-\delta}$ were synthesized by solid state synthesis method under identical conditions. Stoichiometric amounts of the precursor powders, $CaCO_3$ (Alfa Aesar, 99.95%), Fe_2O_3 (Alfa Aesar, 99.998%), Mn_2O_3 (Alfa Aesar, 99.998%) and

$SrCO_3$ (Sigma Aldrich, 99.99%) were mixed together using an agate mortar and pestle and pressed into pellets which were calcined in air at 1000 °C for 24 h. The samples were then ground and sintered at 1200 °C for 24 h in the same condition, followed by slow cooling. The heating and cooling rates were 100 °C/h in each heating cycle. A previous report[18] on $Ca_2FeMnO_{6-\delta}$ indicates the presence of a small amount of impurities only in this material, which was also observed in the current work. The structure of polycrystalline samples was examined by powder X-ray diffraction (XRD) at room temperature using Cu Kα1 radiation (λ = 1.54056 Å). Rietveld refinements were performed using GSAS software[20] and EXPEGUI interface.[21] The sample morphologies were studied using high resolution field-emission scanning electron microscopy (SEM).

Oxygen content of each material was determined by iodometric titration as described elsewhere.[22] About 50 mg of the sample and excess KI (~2 g) were dissolved in 100 mL of 1M HCl. A total of 5 mL of the solution was then pipetted out in a conical flask and 20mL of degassed pure water was added. The whole solution was then titrated against 0.025 M $Na_2S_2O_3$. Near the end point of the titration, 0.2 mL of a starch solution was added to act as an indicator. All steps were performed under argon atmosphere.

The electrical properties were investigated by 4-point probe measurements on as-prepared pellets. Electrical conductivity was measured at different temperatures from 25 to 800 ºC during both heating and cooling cycles. The rate of heating and cooling for conductivity measurements was 3 °C/min.

Electrocatalytic activity measurements were carried out using the typical procedures commonly used in HER/OER catalysis. [1, 7, 23-29] These measurements were done on an electrochemical workstation in a three-electrode glass cell system. A glassy carbon electrode coated with the catalyst, a commercial platinum electrode and a silver/silver chloride electrode were used as working, counter and reference electrodes, respectively. Control experiments were also done with carbon counter electrode to eliminate the possibility of dissolution of platinum

counter electrode and its contribution to HER.[29] The results from both platinum and carbon counter electrodes were similar (Figure S1). For working electrode preparation, 35 mg of the sample was used, to which 20 µL of nafion was added. 7 mg of carbon powder was also added and stirred for five minutes. 7 mL of THF was then added and stirred for 5 more minutes and then sonicated for 5 minutes. The catalyst ink (4 coats of 10 µL each) was loaded on a glassy carbon electrode with a diameter of 5 mm (area = 0.196 cm^2) with a mass loading of 1.02 mg/cm^2. Before starting each measurement, the electrolyte was bubbled with argon gas for at least 30 minutes. For HER, the voltage window was 0.0 to –0.55 V (vs RHE) with scan rate of 10 mV s^{-1}, using Ag/AgCl (saturated KCl) reference electrode, as commonly utilized in HER.[24-25] For OER, the voltage range of 0.0 - 0.8 V vs Ag/AgCl electrode (in 3 M NaCl) with scan rate of 10 mV s^{-1} was used as commonly utilized in OER experiments.[1, 23] Experiments with lower mass loading of catalyst were also done, as shown in Figure S2. Control experiments were also performed where only carbon ink was loaded onto the electrode (using the same method as before, but without adding the catalytic sample). Running the experiments under either OER or HER conditions using only carbon ink led to negligible activity, as shown in Figure S3. Data were also obtained for OER and HER reference catalysts, RuO_2 and Pt/C (20 wt. % Pt), respectively. Some researchers prefer 46% Pt on carbon.[29] However, many HER studies utilize 20% Pt on carbon.[11, 30-34] All potential values were *iR*-corrected. Chronopotentiometry was employed to study the stability in various electrolytes using a two-electrode method described in the literature,[26] The electrodes were prepared by dropcasting catalyst ink on 1 cm^2 nickel foam. 100 µL of the ink was pipetted and dropcasted on nickel foam in 20 µL increments with a total mass loading of ~ 1 mg/cm^2, followed by air drying overnight. Two such electrodes were prepared. Then gold leads attached to gold wires were attached to the electrodes, which were dipped into 0.1 M or 1 M KOH for stability studies. A glass fiber filter paper was used in between the electrodes to prevent short circuiting and crossover.[27] For stability tests in acidic condition glassy carbon electrode was used, given that nickel foam reacts with acid. All

potential values was converted to be expressed against the reversible hydrogen electrode (RHE) according to Nernst equation, where $E^{o}_{Ag/AgCl}$ = 0.21 V for 3M KCl[28] and 0.197 V for saturated KCl[24] :

$$E_{RHE} = E_{Ag/AgCl} + 0.059\ pH + E^{o}_{Ag/AgCl} \qquad (1)$$

For OER, gas chromatography experiments were also done to confirm the formation of oxygen (Figure S4). Before starting the electrolysis, the electrolyte was purged with nitrogen for 60 minutes. The electrolyte was then stirred during electrolysis. Prior to applying any potential, chromatograms were obtained to show that the cell has been purged and contained no ambient oxygen. A constant potential of 0.62 V vs Ag/AgCl was then applied and data were collected at 30, 45, and 60 minutes of the OER. Oxygen gas was detected by online automatic injection (1 mL sample) using a thermal conductivity detector. The carrier gas for the column was nitrogen. The gas was injected every 15 minutes.

RESULTS AND DISCUSSION

Crystal Structure

In oxygen-deficient perovskites, $ABO_{3-\delta}$ or $A_2B_2O_{6-\delta}$, the cations on the B-site often have octahedral, square-pyramidal or tetrahedral coordination geometry,[16-17] while the larger A-cations reside in spaces between the above polyhedra. In this class of materials, the vacancies, created due to oxygen-deficiency, can have either random or ordered distribution. The variation in the arrangement of oxygen-vacancies is a primarily factor that leads to different structures and various coordination geometries for B-site cations. The oxygen-deficient perovskites studied in this work, $Sr_2FeMnO_{6-\delta}$, $CaSrFeMnO_{6-\delta}$ and $Ca_2FeMnO_{6-\delta}$, show variation in crystal structure (Figure 1) due to the change in the ionic radius of the A-site cation, leading to different arrangements of oxygen-vacancies. It is noted that all three materials are synthesized under

identical conditions. Therefore, the structural changes between them are a function of the A-site cation.

Our Rietveld refinements (Figure 1) confirm the previously reported crystal structures.[18-19] In $Ca_2FeMnO_{6-\delta}$, the oxygen-vacancies are distributed in an ordered arrangement and only appear in alternating layers, leading to an orthorhombic *Pnma* structure. The structure consists primarily of alternating FeO_4 tetrahedra and MnO_6 octahedra (Figure 1).[18] The FeO_4 tetrahedra form chains that are sandwiched between MnO_6 octahedral layers. The degree of oxygen-deficiency is determined by iodometric titration, which indicates $\delta \approx 1$ for this compound.

Conversely, in $CaSrFeMnO_{6-\delta}$ and $Sr_2FeMnO_{6-\delta}$, the oxygen-vacancies are disordered,[18-19] and the average structure resembles that of a regular perovskite (Figure 1), but with partial occupancy on oxygen sites. The space group is cubic *Pm*-3*m* and there is no ordering in the structure, as confirmed by Rietveld refinements (Figure 1). Ca and Sr are on the same crystallographic site (0,0,0), and Fe and Mn also share the same position (½,½,½). The degree of oxygen-deficiency is different in these two compounds, $\delta = 0.57$ for $CaSrFeMnO_{6-\delta}$ and $\delta = 0.22$ for $Sr_2FeMnO_{6-\delta}$, as determined by iodometric titrations. Furthermore, the Fe(Mn)–O bond distances are shorter in $CaSrFeMnO_{6-\delta}$, 1.9062(1) Å, compared with those of $Sr_2FeMnO_{6-\delta}$, 1.92526(7) Å.

These results are consistent with previous neutron scattering studies, which have shown the perovskite-type average structure for $CaSrFeMnO_{6-\delta}$ and $Sr_2FeMnO_{6-\delta}$,[18] but with partial occupancy on oxygen sites, indicating long-range disordered arrangement of vacancies. However, neutron pair distribution function analyses[35-36] have shown that at the local level there are domains where the vacancies are ordered in these long-range disordered systems. For $Ca_2FeMnO_{6-\delta}$, neutron scattering studies[18, 37] have indicated long-range vacancy order, evident from conversion of the octahedral geometry into tetrahedral in alternating layers (i.e., the vacancies only appear in alternating layers).

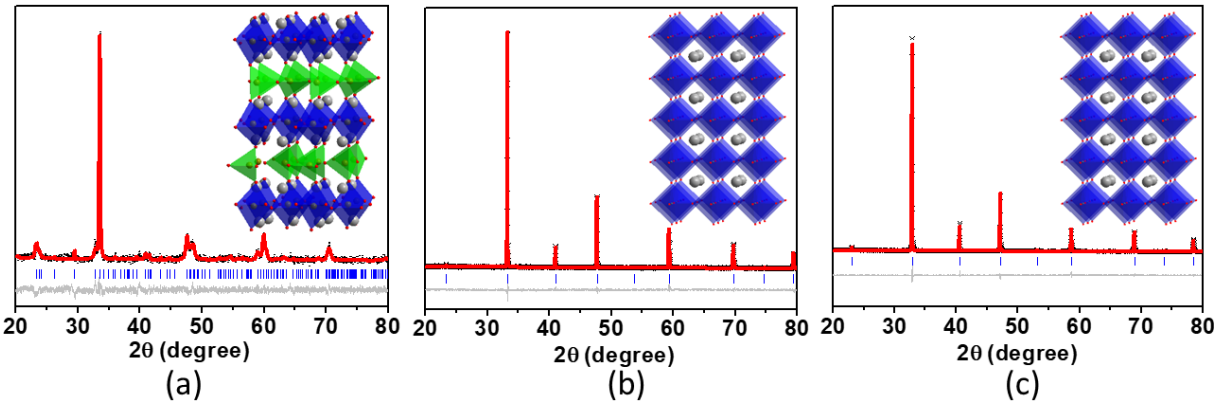

Figure 1. Rietveld refinement profiles for powder X-ray diffraction data of (a) $Ca_2FeMnO_{6-\delta}$, *Pnma*, a = 5.3350(8) Å, b = 14.957(4) Å, c = 5.460(2) Å (b) $CaSrFeMnO_{6-\delta}$, *Pm*-3*m*, a = 3.8124(2) Å and (c) $Sr_2FeMnO_{6-\delta}$, *Pm*-3*m*, a = 3.8505(4) Å. In the insets, $(Fe/Mn)O_6$ octahedra are shown in blue, FeO_4 tetrahedra are in green, and Ca/Sr atoms are represented by gray spheres.

The microstructure of the three materials is also different, as demonstrated by scanning electron microscopy micrographs of the sintered pellets (Figure 2). $Ca_2FeMnO_{6-\delta}$ shows the largest grains among the three compounds. In addition, significant degree of porosity is observed in this material. The grain size for $CaSrFeMnO_{6-\delta}$ and $Sr_2FeMnO_{6-\delta}$ is similar, but the latter shows somewhat higher degree of porosity.

A measure of the relative porosity can also be found using saturation method,[38] In this method, a solid sintered pellet was weighed before (W_{dry}) and after being submerged (W_{sat}) in boiling water for 2 hours in order to determine the amount of fluid that filled the pores of each sample. The percent mass of fluid in pores provides a measure of the porosities of different samples relative to each other:

$$\% \text{ mass of water in pores} = \frac{W_{sat} - W_{dry}}{W_{dry}} \times 100 \qquad (2)$$

The percent mass of fluid in pores is 8.7%, 6.3%, and 7.8% for $Ca_2FeMnO_{6-\delta}$, $CaSrFeMnO_{6-\delta}$, and $Sr_2FeMnO_{6-\delta}$, respectively. This trend in porosity is the same as that observed from SEM. We assign the change in porosity to the variation in sinterability, where an intermediate degree of Ca incorporation leads to optimum sinterability. The change in

sinterability as a function of change in the A-site cation in perovskite-based oxides has been observed previously.[39]

The structural dissimilarities between the three materials, in particular the changes in distribution of oxygen-vacancies and the ensuing structural order/disorder, give rise to significant differences in electrical charge-transport, as well as electrocatalytic properties. As will be discussed in detail in next sections, the vacancy-ordered compound, $Ca_2FeMnO_{6-\delta}$, has the least electrocatalytic activity, whereas the disordered compounds, $Sr_2FeMnO_{6-\delta}$ and $CaSrFeMnO_{6-\delta}$, are significantly more active, with latter material showing the most activity. It is also noted that among the two disordered structures that have good electrocatalytic activity, the degree of oxygen deficiency, δ, for the most active material, $CaSrFeMnO_{6-\delta}$ ($\delta = 0.57$), is greater than that of $Sr_2FeMnO_{6-\delta}$ ($\delta = 0.22$). This effect, *i.e.*, the impact of oxygen vacancies on electrocatalytic activity, has been demonstrated for other oxides before.[4, 6, 40]

The cooperative effect due to the presence of both Ca and Sr in $CaSrFeMnO_{6-\delta}$ should also be noted. The synergetic effect between Ca/Sr on the A-site and Fe/Mn on the B-site can lead to the enhanced electrocatalytic activity, similar to the cooperative coupling effect observed previously in some perovskites.[41] Furthermore, the compositional and structural changes lead to significant variation in electrical conductivity, which in turn affect the electrocatalytic activity. In fact, the trend in electrical conductivity matches nicely with the trend in electrocatalytic activity, as will be discussed later in connection with structural properties.

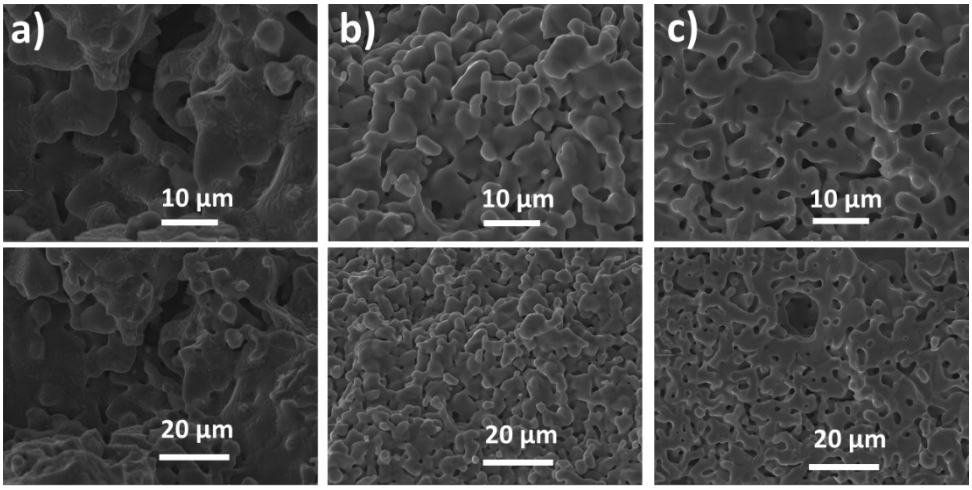

Figure 2. Scanning electron microscopy images of (a) $Ca_2FeMnO_{6-\delta}$ (b) $CaSrFeMnO_{6-\delta}$ and (c) $Sr_2FeMnO_{6-\delta}$. Note that $Ca_2FeMnO_{6-\delta}$ has the largest grains and highest porosity. The grain size for $CaSrFeMnO_{6-\delta}$ and $Sr_2FeMnO_{6-\delta}$ is similar, but the latter has somewhat higher porosity.

Hydrogen-Evolution Activity

Researchers have studied HER in either acidic or basic media depending on the catalyst. As described before, most of the catalysts utilized for HER are non-oxide materials. In acidic condition, materials such as sulphides[12, 42], carbides[9], nitrides[9], and metals[43] have been used. Similarly, in basic medium, catalysts such as sulphides[44], phosphides[13], carbides[9] and nitrides[9] have been utilized. Very few oxides have shown HER activity in either acidic[14] or alkaline[15] environment. Recently, a perovskite oxide has been studied for HER in 1 M KOH.[8] The electrocatalytic activity of perovskite oxides for HER in acidic environment is even less common. One study that briefly studied a perovskite oxide, reproted very low HER acitivty in acidic medium.[45] In general, it is uncommon to find bulk oxide materials that exhibit HER activity both in acidic and basic media. In fact, no perovskite oxide with such property has been reported to date. However, the materials studied in this work show HER activity in both conditions, as described below.

Given that HER experiments are frequently done in 0.5 M H_2SO_4 or 1 M KOH,[9, 15, 24, 46-47] the same conditions were used in the study of the HER activities of $Ca_2FeMnO_{6-\delta}$, $CaSrFeMnO_{6-\delta}$, and $Sr_2FeMnO_{6-\delta}$. Figure 3 shows the polarization curves of the three materials, as well as that of the reference Pt/C catalyst (20 wt. % Pt). The onset potential, where the HER

process commences, and the overpotential at 10 mA/cm^2 are frequently used as indications of catalysts performance.[48-49] The reference Pt/C catalyst shows onset potential of almost zero, as expected.[8-10] The HER activities of our materials show the following order: $Ca_2FeMnO_{6-\delta}$ < $Sr_2FeMnO_{6-\delta}$ < $CaSrFeMnO_{6-\delta}$. Among the three compounds, $CaSrFeMnO_5$ shows the best (lowest) onset potential and overpotential in both acidic and basic conditions. It also shows the best mass activity, 43.5 A/g in acidic condition and 13.5 A/g in basic condition at –0.3 V. Whereas, the mass activities for the other two compounds are in the range of 3.0 A/g to 5.5 A/g at –0.3 V.

The onset potential values for $CaSrFeMnO_{6-\delta}$ are –0.10 V vs RHE in acidic condition, and –0.14 V vs RHE in basic condition. Its overpotential values at 10 mA/cm^2 are –0.31 V and –0.39 V vs RHE in acidic and basic conditions, respectively. While there are some oxides, such as $Pr_{0.5}BSCF$[8] and $PrBaCo_2O_{5+\delta}$[50], that show better HER performance in basic condition, the remarkable feature of $CaSrFeMnO_{6-\delta}$ is its ability to catalyze HER in both acidic and alkaline conditions. Furthermore, its HER activity in acidic condition, is superior to those of gold[51], boron nitride/GC[51], WO_3[52], and the widely studied MoS_2[53] in acidic condition. It is also superior to the activity of MoS_2 in alkaline medium.[54]

The better performance in acidic condition can be attributed to relatively higher energy requirement for the proton generation in alkaline solution.[55] Enhanced HER activity in acidic condition compared with basic environment has been observed for another catalyst before.[24] Nevertheless, it is important to note that oxide HER catalysts capable of functioning in both acidic and basic conditions are uncommon.

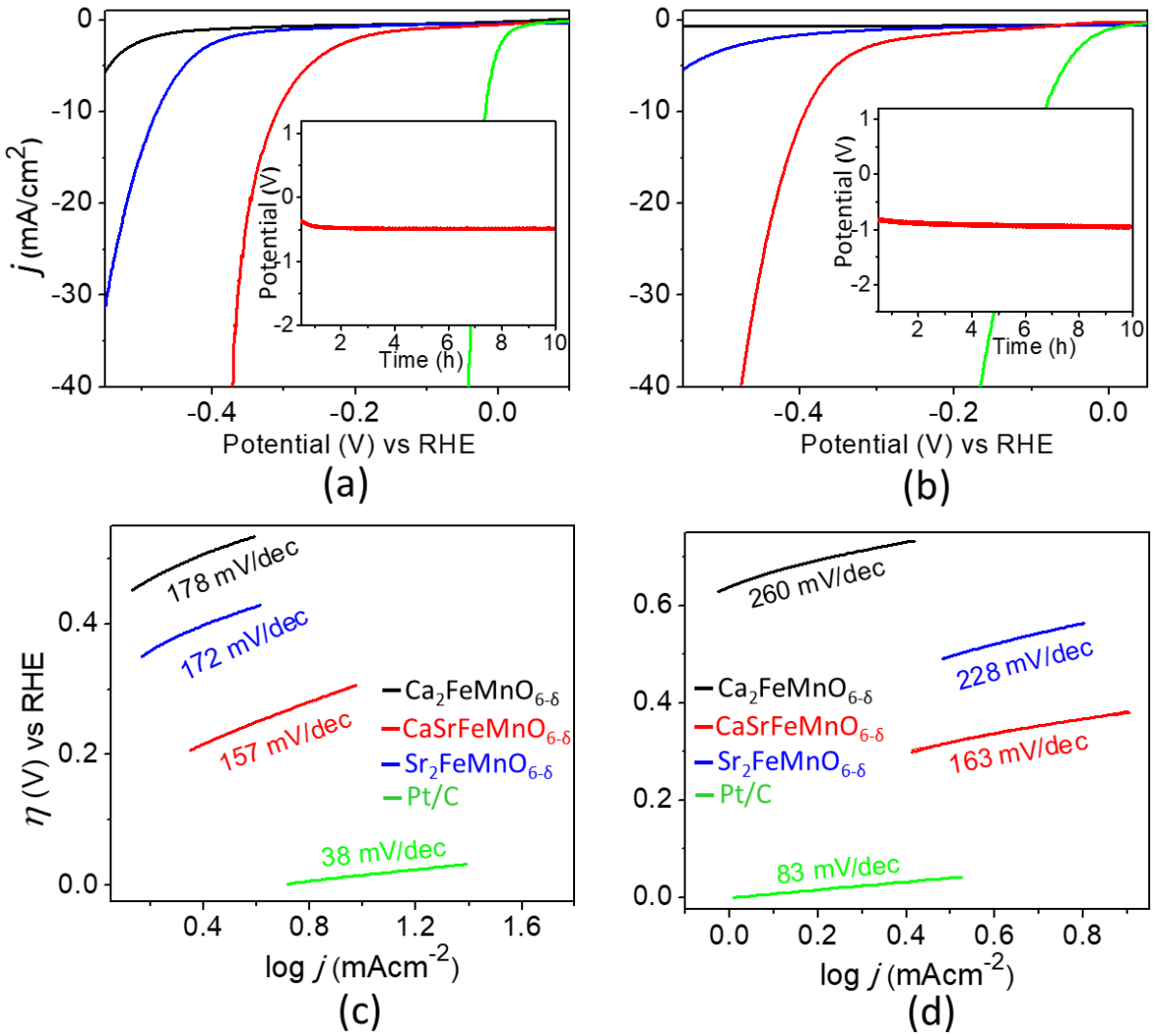

Figure 3. (a) and (b) show HER polarization curves in acidic and basic conditions, respectively. Pt/C data are shown in green, $Ca_2FeMnO_{6-\delta}$ in black, $CaSrFeMnO_{6-\delta}$ in red, and $Sr_2FeMnO_{6-\delta}$ in blue. Inset presents chronopotentiometry data, showing the stability of the best catalyst, $CaSrFeMnO_{6-\delta}$, as a function of time. (c) and (d) show Tafel slopes for HER in acidic and basic media, respectively. $CaSrFeMnO_{6-\delta}$ is the best catalyst in the series, with lowest Tafel slope and overpotential.

The kinetics of the HER reaction was also investigated. Tafel slope is generally utilized to study the HER kinetics, which is evaluated using Tafel equation:[15]

$$\eta = a + b \log j \qquad (3)$$

where η is overpotential, and j is current density. The slope of the plot of η versus $\log j$ is indicative of the reaction rate (Figures 3c and 3d). The smaller the slope, the faster the reaction. The Tafel slope of the reference Pt/C catalyst is also shown, matching those reported before in acidic and basic conditions.[9]

The reaction kinetics follow the same trend as catalytic performance, with $CaSrFeMnO_{6-\delta}$ exhibiting the best kinetics and smallest Tafel slope, 157 mV/dec in acidic condition, and 163 mV/dec in basic condition. The relatively large Tafel slopes can be indicative of the mixed HER mechanism. It is known that the HER mechanism involves an initial binding between the catalyst and hydrogen atom (either from H_2O or H_3O^+) depending on the condition, i.e., basic or acidic. This is the Volmer reaction, which is then followed by either Heyrovsky or Tafel reaction. Either of these reactions can be the rate-determining step, resulting in a different Tafel slope, which is expected to have respective values of 120 mV/dec, 40 mV/dec and 30 mV/dec if the rate-determining reaction is Volmer, Heyrovsky or Tafel.[56] However, the Tafel slope can have a different value if more than one of the three steps are the rate-determining reactions. For example, the Mo_2C film shows Tafel slope of 166 mV/dec, which is qualitatively attributed to having two or three rate-determining steps.[56] Similarly large Tafel slopes have also been reported for MoS_2/graphene,[57] surface-functionalized MoS_2 nanosheets,[58] P-doped NiMoO4,[59] and Co/NBC,[60] indicating the mixed mechanism.

The electrochemically active surface area (ECSA) is often evaluated through determination of double layer capacitance, C_{dl}, in the non-faradaic region (Figures S5 and S6).[61] Given the direct proportionality between the two,[62] the C_{dl} value is often taken as a measure of ECSA.[62] The magnitude of C_{dl} is obtained from the slope of Δj, which is the average of j_{anodic} and $j_{cathodic}$ absolute values at middle potential of the CV, versus scan rate, ν, according to the equation:

$$C_{dl} = \Delta j/\nu \qquad (4)$$

As shown in Figure S6, the most active catalyst, $CaSrFeMnO_{6-\delta}$, also has the largest C_{dl} in both acidic and basic media.

Oxygen-Evolution Activity

Remarkably, in addition to HER activity, all of our three materials show catalytic activity for OER (Figure 4). Given that most reports on OER electrocatalysis are in 0.1 M KOH, the same conditions were used for our materials to allow direct comparison to other reported catalysts. However, experiments in the same conditions as those of HER, namely 1 M KOH and 0.5 M H_2SO_4 were also performed. The OER tests in acidic condition (0.5 M H_2SO_4) led to very high overpotentials, while OER experiments in 1 M KOH resulted in reasonable activity, but still less than the activity in 0.1 M KOH. The results for 0.1 M KOH are described here to allow comparison to previously reported catalysts. The most structurally ordered compound, $Ca_2FeMnO_{6-\delta}$, shows the lowest OER activity, while the best performance is observed for $CaSrFeMnO_{6-\delta}$. This is the same trend observed in the HER activity of these materials. In OER experiments the onset potential in cyclic voltammetry, where the reaction commences, as well as the overpotential, η, beyond the ideal 1.23 V, are important parameters that are commonly used to evaluate the activity of catalysts. The overpotential is usually evaluated at 10 mA/cm^2, which has been adopted as a convention for comparing different catalysts.[63] The three compounds show onset potentials of ~1.45 V to 1.50 V in 0.1 M KOH. The overpotential at 10 mA/cm^2 varies significantly, from $\eta \approx 0.56$ V for $Ca_2FeMnO_{6-\delta}$, to $\eta \approx 0.37$ V for $CaSrFeMnO_{6-\delta}$, and $\eta \approx 0.42$ V for $Sr_2FeMnO_{6-\delta}$ (Figure 4).

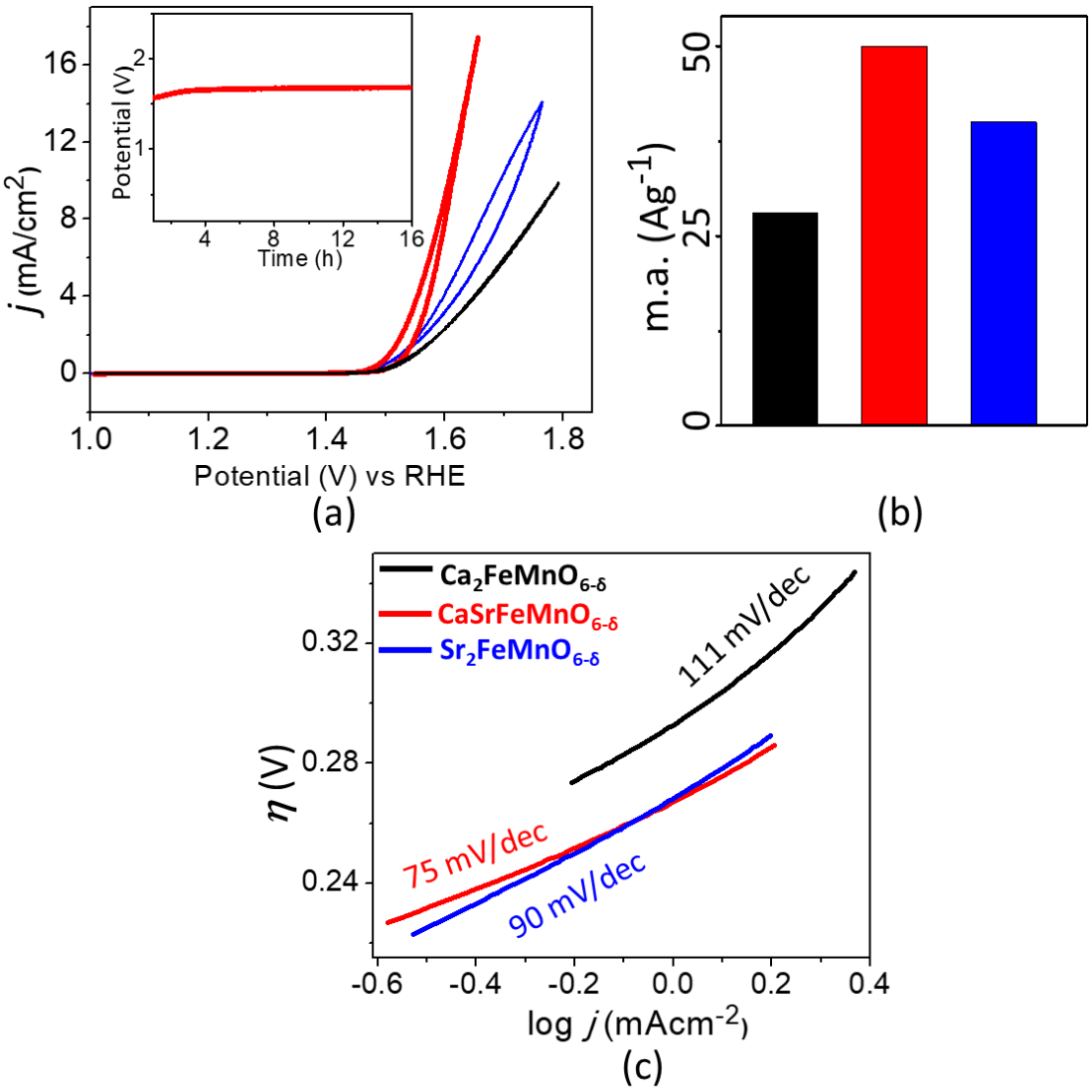

Figure 4. (a) OER polarization curves in 0.1 M KOH. Inset presents chronopotentiometry data, showing the stability of the best catalyst, $CaSrFeMnO_{6-\delta}$, as a function of time. (b) Mass activities at 1.7 V in 0.1 M KOH. (c) Tafel slopes indicating the OER kinetics. Data for $Ca_2FeMnO_{6-\delta}$ are shown in black, $CaSrFeMnO_{6-\delta}$ in red, and $Sr_2FeMnO_{6-\delta}$ in blue. $CaSrFeMnO_{6-\delta}$ is the best catalyst in the series, with lowest Tafel slope and overpotential.

The mass activity (A/g) was also calculated using the catalyst loading mass (0.1 mg cm^{-2}) and the measured current density J (mA cm^{-2}). Figure 4b compares the OER mass activities of these materials at 1.70 V vs RHE. $CaSrFeMnO_{6-\delta}$ shows significantly greater mass activity (~50 A/g) than $Sr_2FeMnO_{6-\delta}$ (~40 A/g) and $Ca_2FeMnO_{6-\delta}$ (~28 A/g). The mass activity of $CaSrFeMnO_{6-\delta}$ and $Sr_2FeMnO_{6-\delta}$ are higher than that of a previously reported Mn-based oxygen-deficient perovskite, $Ca_2Mn_2O_5$, 30.1 A/g at 1.7 V.[4]

The kinetics of OER was also investigated for all three materials. Similar to HER,

Tafel slope is frequently utilized to study the OER kinetics based on equation (3) (Tafel equation), $\eta = a + b \log j$ [62, 64] where η is the overpotential, and j is the current density, as previously discussed. The kinetics, represented by the Tafel plot, η vs. log j, is affected by electron and mass transport.[65-66] Thus, Tafel plot can provide information about electronic transport in electrocatalysts.[66] Smaller slope of Tafel plot indicates faster reaction and better kinetics of OER. The Tafel slopes for $Ca_2FeMnO_{6-\delta}$, $CaSrFeMnO_{6-\delta}$ and $Sr_2FeMnO_{6-\delta}$ are 111 mV/dec, 75 mV/dec and 90 mV/dec, respectively, as shown in Figure 4c. The smaller Tafel slop of $CaSrFeMnO_{6-\delta}$ is indicative of faster OER kinetics and is consistent with its high electrocatalytic activity.

The comparison of electrocatalytic activity of the materials described in this work with those reported for precious metal catalysts, IrO_2 and RuO_2, indicates the remarkable OER performance of these new electrocatalysts. The catalyst $CaSrFeMnO_{6-\delta}$, described in this work, shows superior OER activity to IrO_2, which has overpotential of $\eta \approx 0.45$ V.[1] It is also superior to RuO_2 (Figure S7), which has a reported overpotential of $\eta \approx 0.42$ V.[2] In addition, it is better than some of the oxide catalysts reported before, such as $SrNb_{0.1}Co_{0.7}Fe_{0.2}O_{3-\delta}$[1] and $Pr_{0.5}Ba_{0.3}Ca_{0.2}CoO_{3-\delta}$.[67]

Furthermore, the kinetics of OER is significantly enhanced by $CaSrFeMnO_{6-\delta}$, as evident from the Tafel slope, 75 mV/dec, compared with that reported for IrO_2, 83 mV/dec.[1] These observations are remarkable, as oxide materials based on earth-abundant metals, which show such high electrocatalytic activity and enhanced kinetics are uncommon.

To examine the stability of catalysts under OER and HER conditions, X-ray diffraction experiments were done before and after 100 cycles of electrocatalytic OER. Similar tests were done before and after 100 cycles of HER. These experiments show that the least electrocatalytically active material, $Ca_2FeMnO_{6-\delta}$, also has the least stability, and disintegrates under OER or HER conditions. The compound with better electrocatalytic performance, $Sr_2FeMnO_{6-\delta}$, shows better stability than $Ca_2FeMnO_{6-\delta}$, but still decomposes under some

electrocatalytic conditions. However, the best electrocatalyst, $CaSrFeMnO_{6-\delta}$, also shows the best stability, retaining its structural integrity in all experimental conditions in this work, as shown in Figure S8. Under these OER and HER conditions, the vacancy-ordered structure of $Ca_2FeMnO_{6-\delta}$ can not be retained, whereas the disordered structure of $Sr_2FeMnO_{6-\delta}$ and $CaSrFeMnO_{6-\delta}$ are more stable. Among $Sr_2FeMnO_{6-\delta}$ and $CaSrFeMnO_{6-\delta}$, the latter has better stability due to the synergetic effect of Ca/Sr. As mentioned before, bond distances in $CaSrFeMnO_{6-\delta}$ are shorter than those in $Sr_2FeMnO_{6-\delta}$, indicating the formation of stronger bonds in $CaSrFeMnO_{6-\delta}$, which may contribute to its stability.

Considering that HER and OER are processes that involve the transfer of electrons, we speculated that the observed trend in electrocatalytic properties of $Ca_2FeMnO_{6-\delta}$, $CaSrFeMnO_{6-\delta}$ and $Sr_2FeMnO_{6-\delta}$ could be related to the electrical charge-transport properties. Therefore, we conducted a thorough investigation of the electrical charge-transport, as described below.

Electrical Conductivity

The semiconducting charge-transport properties in some oxygen-deficient perovskites have been demonstrated before.[68-70] In materials where electronic conductivity is dominant, the semicircles in AC conductivity data can sometimes disappear, and only a straight line is observed.[71-72] In these situations, the intercept of the line on the x-axis gives the total resistance,[71] and is expected to match the resistance from the DC measurements. This property was observed for the materials studied in this work. The resistance values (R) obtained from AC and DC measurements were used to calculate the conductivity (σ) using the equation:[73]

$$\sigma = L/RA \qquad (5)$$

where L and A represent the voltage-probe spacing in 4-probe set-up and cross-sectional area of the rectangular sample, respectively. The electrical conductivity of $CaSrFeMnO_{6-\delta}$ (4.31×10^{-1} Scm^{-1} at 25 °C and 122×10^{2} Scm^{-1} at 800 °C) was found to be 1-2 orders of magnitude

greater than those of $Sr_2FeMnO_{6-\delta}$ (2.07 x 10^{-2} Scm^{-1} at 25 °C and 5.40 Scm^{-1} at 800 °C) and $Ca_2FeMnO_{6-\delta}$, (2.59 x 10^{-3} Scm^{-1} at 25 °C and 3.68 Scm^{-1} at 800 °C), as shown in Figure 5. The applied potential in these measurements was 10 mV. It should be recognized that electrical conductivity is potential-dependent, and its absolute value can vary depending on the potential. Nevertheless, the important observation here is the systematic trend in electrical conductivity of the three materials, $Ca_2FeMnO_{6-\delta}$, $CaSrFeMnO_{6-\delta}$ and $Sr_2FeMnO_{6-\delta}$.

This remarkable difference can arise from structural differences. In perovskite-based oxides, transition metals with variable oxidation states, such as Fe and Mn, are responsible for electronic conductivity. Electron hopping takes place through the M–O–M bond system,[74-75] where M represents the transition metal. The electronic conductivity depends on various factors such as the M–O–M bond angle,[76-77] which appears to be a dominant structural parameter.[27] As the M–O–M bond angle becomes larger and gets closer to 180°, the M 3d and O 2p orbitals become more axially aligned, leading to better overlap and enhanced conductivity.[78] Given the corner-sharing connectivity of both tetrahedra and octahedra in $Ca_2FeMnO_{6-\delta}$, the bond angles in this compound are highly distorted, and can be as small as ~130°, which can impede the orbital overlap, and electrical conductivity. The bond angles in $Sr_2FeMnO_{6-\delta}$ and $CaSrFeMnO_{6-\delta}$ are much larger, 180°. Therefore, better orbital overlap is expected. However, the (FeMn)–O bond distances in $CaSrFeMnO_{6-\delta}$, 1.9062(1) Å, are shorter than those in $Sr_2FeMnO_{6-\delta}$, 1.92526(7) Å, which can enhance the overlap of M 3d and O 2p orbitals,[76-77] leading to greater conductivity. The effect of bond distance has been previously observed for other perovskite oxides.[76-77] Furthermore, the concentration of defects in $CaSrFeMnO_{6-\delta}$, $\delta = 0.57$, is greater than that of $Sr_2FeMnO_{6-\delta}$, $\delta = 0.22$. This can be another reason for the higher conductivity of $CaSrFeMnO_{6-\delta}$. A similar effect, namely variation of the defect-concentration, was recently reported for another series of perovskite-based oxides.[17]

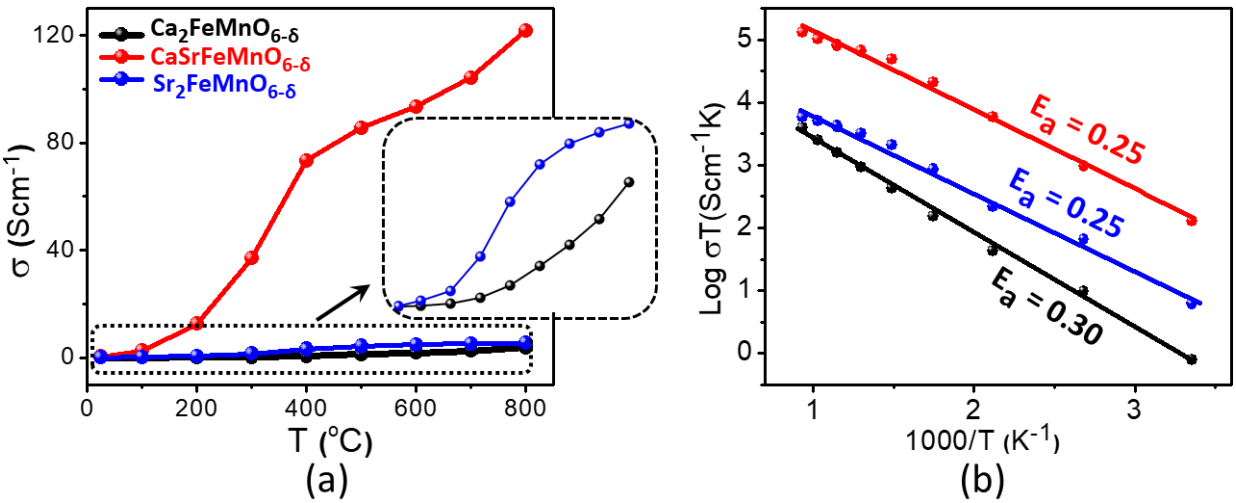

Figure 5. (a) Temperature-dependent electrical conductivity of $Ca_2FeMnO_{6-\delta}$ (black), $CaSrFeMnO_{6-\delta}$ (red) and $Sr_2MnO_{6-\delta}$ (blue). (b) Arrhenius plots and activation energies. In this series, $CaSrFeMnO_{6-\delta}$ shows the highest conductivity in the entire range of 25 – 800 °C.

The temperature-dependent conductivity of these materials was also studied in a wide temperature-range, from 25 – 800 °C (Figure 5a). These data can be used to calculate the activation energy using Arrhenius equation for thermally activated conductivity:[79-81]

$$\sigma T = \sigma^{o} e^{\frac{-E_a}{KT}} \qquad (6)$$

where σ° is a preexponential factor and a characteristic of the material. E_a, K, and T are the activation energy for the electrical conductivity, Boltzmann constant, and absolute temperature, respectively. The activation energy (E_a) can be calculated from the slope of the line of best fit in the log σT vs. $1000/T$ plot, as shown in Figure 5b. All compounds show an increase in conductivity as a function of temperature, indicative of their semiconducting nature. As temperature rises, there is an increase in the mobility of charge-carriers, which leads to the increase in conductivity. The relation between conductivity and the mobility of charge-carriers for temperature-activated conductivity in semiconductors can be represented as[82] $\sigma = ne\mu$, where σ, n, e, and μ are the conductivity, concentration of charge-carriers, charge of the electron, and mobility of the charge-carriers, respectively. As shown in Figure 5a, the superior conductivity of $CaSrFeMnO_{6-\delta}$ persists in the entire temperature-range. The trend in electrical charge transport, shown in Figure 5, is the same as the trend in HER and OER activity. As

discussed above, charge-transport is in turn controlled by compositional and structural characteristics of materials. Table S1 shows a comparison of properties of the three compounds.

The effect of electrical conductivity on electrocatalytic activity is demonstrated by other researchers as well.[83-87] For example, the effect of conductive substrates on the OER activity of an oxyhydroxide has been shown,[86] where the formation of conductive gold oxide on the surface of gold substrate is proposed to result in better OER activity compared with platinum substrate that does not form a conductive oxide.[86] However, gold and platinum are not commonly used as substrates in electrocatalytic OER or HER. Another study on the essential role of electrical conductivity in electrocatalysis demonstrates that the improvement of charge-transport upon nanostructuring of an insulating material results in a significant enhancement of OER activity.[87] This is because nanostructuring enables tunneling mechanism, resulting in an improved charge-transport, leading to enhanced OER.[87]

CONCLUSION

The extraordinary combination of properties observed in above materials, namely their ability to act as bifunctional electrocatalysts for both OER and HER, and the capability to catalyze HER in both acidic and basic media, is unprecedented. The structure-property relationships demonstrated by these materials is notable, where the disparity in structural properties leads to significant variations in electrical charge-transport and electrocatalytic activity. The structural properties are the underlying basis for the catalytic properties of the best catalyst in the series, $CaSrFeMnO_{6-\delta}$, which not only catalyzes both HER and OER, but also shows superior catalytic performance to the state-of-the-art precious-metal catalysts.

Supporting Information. X-ray diffraction data before and after electrocatalysis, normalized electrocatalysis data, double layer capacitance and related CVs, gas chromatography data, OER

data for RuO_2, and control experiment results using only carbon black, different catalyst mass loadings, or with carbon counter electrode.

Acknowledgement

This work is supported in part by the National Science Foundation under Grant No. DMR-1943085.

Conflict of Interests

The authors declare no conflict of interests

References

1. Zhu, Y.; Zhou, W.; Chen, Z. G.; Chen, Y.; Su, C.; Tadé Moses, O.; Shao, Z., $SrNb_{0.1}Co_{0.7}Fe_{0.2}O_{3-\delta}$ perovskite as a next-generation electrocatalyst for oxygen evolution in alkaline solution. *Angew. Chem., Int. Ed.* **2015,** *54*, 3897, doi.org/10.1002/ange.201408998.
2. Das, D.; Das, A.; Reghunath, M.; Nanda, K. K., Phosphine-free avenue to Co_2P nanoparticle encapsulated N,P co-doped CNTs: a novel non-enzymatic glucose sensor and an efficient electrocatalyst for oxygen evolution reaction. *Green Chem.* **2017,** *19*, 1327-1335, doi.org/10.1039/C7GC00084G.
3. Kwon, T.; Hwang, H.; Sa, Y. J.; Park, J.; Baik, H.; Joo, S. H.; Lee, K., Cobalt Assisted Synthesis of IrCu Hollow Octahedral Nanocages as Highly Active Electrocatalysts toward Oxygen Evolution Reaction. *Adv. Funct. Mater.* **2017,** *27*, 1604688, doi.org/10.1002/adfm.201604688.
4. Kim, J.; Yin, X.; Tsao, K. C.; Fang, S.; Yang, H., $Ca_2Mn_2O_5$ as oxygen-deficient perovskite electrocatalyst for oxygen evolution reaction. *J. Am. Chem. Soc.* **2014,** *136*, 14646-14649, doi.org/10.1021/ja506254g.
5. Lee, J. G.; Hwang, J.; Hwang, H. J.; Jeon, O. S.; Jang, J.; Kwon, O.; Lee, Y.; Han, B.; Shul, Y.-G., A new family of perovskite catalysts for oxygen-evolution reaction in alkaline media: $BaNiO_3$ and $BaNi_{0.83}O_{2.5}$. *J. Am.Chem. Soc.* **2016,** *138*, 3541-3547, doi.org/10.1021/jacs.6b00036.
6. Hona, R. K.; Ramezanipour, F., Remarkable Oxygen-Evolution Activity of a Perovskite Oxide from the $Ca_{2-x}Sr_xFe_2O_{6-\delta}$ Series. *Angew. Chem. Int. Ed.* **2019,** *58*, 2060-2063, doi.org/10.1002/anie.201813000.
7. Suntivich, J.; May, K. J.; Gasteiger, H. A.; Goodenough, J. B.; Shao-Horn, Y., A perovskite oxide optimized for oxygen evolution catalysis from molecular orbital principles. *Science* **2011,** *334*, 1383-1385, DOI: 10.1126/science.1212858.
8. Xu, X.; Chen, Y.; Zhou, W.; Zhu, Z.; Su, C.; Liu, M.; Shao, Z., A Perovskite Electrocatalyst for Efficient Hydrogen Evolution Reaction. *Adv. Mater.* **2016,** *28*, 6442-6448, doi.org/10.1002/adma.201600005.
9. Ma, L.; Ting, L. R. L.; Molinari, V.; Giordano, C.; Yeo, B. S., Efficient hydrogen evolution reaction catalyzed by molybdenum carbide and molybdenum nitride nanocatalysts

synthesized via the urea glass route. *J. Mater. Chem. A* **2015,** *3*, 8361-8368, doi.org/10.1039/C5TA00139K.
10. Zhu, Y.; Zhou, W.; Zhong, Y.; Bu, Y.; Chen, X.; Zhong, Q.; Liu, M.; Shao, Z., A Perovskite Nanorod as Bifunctional Electrocatalyst for Overall Water Splitting. *Adv. Energy Mater.* **2017,** *7*, 1602122, doi.org/10.1002/aenm.201602122.
11. Kim, S.-j.; Jung, H.; Lee, C.; Kim, M. H.; Lee, Y., Comparative Study on Hydrogen Evolution Reaction Activity of Electrospun Nanofibers with Diverse Metallic Ir and IrO_2 Composition Ratios. *ACS Sustainable Chem. Eng.* **2019,** *7*, 8613-8620, doi.org/10.1021/acssuschemeng.9b00402.
12. Zhang, C.; Wang, Z.; Bhoyate, S.; Morey, T.; Neria, B. L.; Vasiraju, V.; Gupta, G.; Palchoudhury, S.; Kahol, P. K.; Mishra, S. R.; Perez, F.; Gupta, R. K., MoS_2 Decorated Carbon Nanofibers as Efficient and Durable Electrocatalyst for Hydrogen Evolution Reaction. *J. Carbon Res.* **2017,** *3*, 33, doi.org/10.3390/c3040033.
13. Yang, F.; Kang, N.; Yan, J.; Wang, X.; He, J.; Huo, S.; Song, L., Hydrogen Evolution Reaction Property of Molybdenum Disulfide/Nickel Phosphide Hybrids in Alkaline Solution. *Metals* **2018,** *8*, 359, doi.org/10.3390/met8050359.
14. Nayak, A. K.; Verma, M.; Sohn, Y.; Deshpande, P. A.; Pradhan, D., Highly Active Tungsten Oxide Nanoplate Electrocatalysts for the Hydrogen Evolution Reaction in Acidic and Near Neutral Electrolytes. **2017,** *2*, 7039-7047, 10.1021/acsomega.7b01151.
15. Hao, Z.; Yang, S.; Niu, J.; Fang, Z.; Liu, L.; Dong, Q.; Song, S.; Zhao, Y., A bimetallic oxide $Fe_{1.89}Mo_{4.11}O_7$ electrocatalyst with highly efficient hydrogen evolution reaction activity in alkaline and acidic media. *Chem. Sci.* **2018,** *9*, 5640-5645, doi.org/10.1039/C8SC01710G.
16. Hona, R. K.; Huq, A.; Mulmi, S.; Ramezanipour, F., Transformation of structure, electrical conductivity, and magnetism in $AA'Fe_2O_{6-\delta}$, A = Sr, Ca and A′ = Sr. *Inorg. Chem.* **2017,** *56*, 9716-9724, doi.org/10.1021/acs.inorgchem.7b01228.
17. Hona, R. K.; Huq, A.; Ramezanipour, F., Unraveling the role of structural order in the transformation of electrical conductivity in $Ca_2FeCoO_{6-\delta}$, $CaSrFeCoO_{6-\delta}$, and $Sr_2FeCoO_{6-\delta}$. *Inorg. Chem.* **2017,** *56*, 14494-14505, doi.org/10.1021/acs.inorgchem.7b02079.
18. Ramezanipour, F.; Greedan, J. E.; Cranswick, L. M. D.; Garlea, V. O.; Donaberger, R. L.; Siewenie, J., Systematic study of compositional and synthetic control of vacancy and magnetic ordering in oxygen-deficient perovskites $Ca_2Fe_{2-x}Mn_xO_{5+y}$and $CaSrFe_{2-x}Mn_xO_{5+y}$ (x = 1/2, 2/3, and 1; y = 0–1/2). *J. Am. Chem. Soc.* **2012,** *134*, 3215-3227, doi.org/10.1021/ja210985t.
19. Ramezanipour, F.; Greedan, J. E.; Siewenie, J.; Proffen, T.; Ryan, D. H.; Grosvenor, A. P.; Donaberger, R. L., Local and average structures and magnetic properties of Sr_2FeMnO_{5+y}, y = 0.0, 0.5. Comparisons with Ca_2FeMnO_5 and the effect of the A-site cation. *Inorg.Chem.* **2011,** *50*, 7779-7791, doi.org/10.1021/ic200919m.
20. Larson, A. C.; Von Dreele, A. C., General structure analysis system (GSAS). *Los Alamos National Laboratory Report LAUR* **1994**, 86 - 748.
21. Toby, B. H., EXPGUI, a graphical user interface for GSAS. *J. Appl. Crystallogr.* **2001,** *34* 210-213, doi.org/10.1107/S0021889801002242.
22. Hona, R. K.; Ramezanipour, F., Disparity in electrical and magnetic properties of isostructural oxygen-deficient perovskites $BaSrCo_2O_{6-\delta}$ and $BaSrCoFeO_{6-\delta}$. *J. Mater. Sci. Mater. Electron.* **2018,** *29*, 13464-13473, 10.1007/s10854-018-9471-8.
23. Xu, X.; Pan, Y.; Zhou, W.; Chen, Y.; Zhang, Z.; Shao, Z., Toward Enhanced Oxygen Evolution on Perovskite Oxides Synthesized from Different Approaches: A Case Study of $Ba_{0.5}Sr_{0.5}Co_{0.8}Fe_{0.2}O_{3-\delta}$. *Electrochim. Acta* **2016,** *219*, 553-559, doi.org/10.1016/j.electacta.2016.10.031.
24. Jia, Y.; Zhang, L.; Du, A.; Gao, G.; Chen, J.; Yan, X.; Brown, C. L.; Yao, X., Defect Graphene as a Trifunctional Catalyst for Electrochemical Reactions. *Adv. Mater.* **2016,** *28*, 9532-9538, doi.org/10.1002/adma.201602912.

25. Martindale, B. C. M.; Reisner, E., Bi-Functional Iron-Only Electrodes for Efficient Water Splitting with Enhanced Stability through In Situ Electrochemical Regeneration. *Adv. Energy Mater.* **2016,** *6*, 1502095, doi.org/10.1002/aenm.201502095.
26. Wang, J.; Gao, Y.; Chen, D.; Liu, J.; Zhang, Z.; Shao, Z.; Ciucci, F., Water Splitting with an Enhanced Bifunctional Double Perovskite. *ACS Catal.* **2018,** *8*, 364-371, doi.org/10.1021/acscatal.7b02650.
27. Ng, J. W. D.; García-Melchor, M.; Bajdich, M.; Chakthranont, P.; Kirk, C.; Vojvodic, A.; Jaramillo, T. F., Gold-supported cerium-doped NiO_x catalysts for water oxidation. *Nat. Energy* **2016,** *1*, 16053, doi.org/10.1038/nenergy.2016.53.
28. Jeerage, K. M.; Candelaria, S. L.; Stavis, S. M., Rapid Synthesis and Correlative Measurements of Electrocatalytic Nickel/Iron Oxide Nanoparticles. *Sci. Rep.* **2018,** *8*, 4584, doi.org/10.1038/s41598-018-22609-x.
29. Wei, C.; Rao, R. R.; Peng, J.; Huang, B.; Stephens, I. E. L.; Risch, M.; Xu, Z. J.; Shao-Horn, Y., Recommended Practices and Benchmark Activity for Hydrogen and Oxygen Electrocatalysis in Water Splitting and Fuel Cells. *Adv. Mater.* **2019,** *31*, 1806296, doi.org/10.1002/adma.201806296.
30. Fang, S.; Zhu, X.; Liu, X.; Gu, J.; Liu, W.; Wang, D.; Zhang, W.; Lin, Y.; Lu, J.; Wei, S.; Li, Y.; Yao, T., Uncovering near-free platinum single-atom dynamics during electrochemical hydrogen evolution reaction. *Nat. Commun.* **2020,** *11*, 1029, doi.org/10.1038/s41467-020-14848-2.
31. Tiwari, J. N.; Sultan, S.; Myung, C. W.; Yoon, T.; Li, N.; Ha, M.; Harzandi, A. M.; Park, H. J.; Kim, D. Y.; Chandrasekaran, S. S.; Lee, W. G.; Vij, V.; Kang, H.; Shin, T. J.; Shin, H. S.; Lee, G.; Lee, Z.; Kim, K. S., Multicomponent electrocatalyst with ultralow Pt loading and high hydrogen evolution activity. *Nat. Energy* **2018,** *3*, 773-782, doi.org/10.1038/s41560-018-0209-x.
32. Mahmood, N.; Yao, Y.; Zhang, J.-W.; Pan, L.; Zhang, X.; Zou, J.-J., Electrocatalysts for Hydrogen Evolution in Alkaline Electrolytes: Mechanisms, Challenges, and Prospective Solutions. *Adv. Sci.* **2018,** *5*, 1700464, doi.org/10.1002/advs.201700464.
33. Liu, Y.; Li, X.; Zhang, Q.; Li, W.; Xie, Y.; Liu, H.; Shang, L.; Liu, Z.; Chen, Z.; Gu, L.; Tang, Z.; Zhang, T.; Lu, S., A General Route to Prepare Low-Ruthenium-Content Bimetallic Electrocatalysts for pH-Universal Hydrogen Evolution Reaction by Using Carbon Quantum Dots. *Angew. Chem. Int. Ed.* **2020,** *59*, 1718-1726, doi.org/10.1002/ange.201913910.
34. Rajala, T.; Kronberg, R.; Backhouse, R.; Buan, M. E. M.; Tripathi, M.; Zitolo, A.; Jiang, H.; Laasonen, K.; Susi, T.; Jaouen, F.; Kallio, T., A platinum nanowire electrocatalyst on single-walled carbon nanotubes to drive hydrogen evolution. *Appl. Catal. B: Environmental* **2020,** *265*, 118582, doi.org/10.1016/j.apcatb.2019.118582.
35. Ramezanipour, F.; Greedan, J. E.; Siewenie, J.; Proffen, T.; Ryan, D. H.; Grosvenor, A. P.; Donaberger, R. L., Local and Average Structures and Magnetic Properties of Sr_2FeMnO_{5+y}, y=0.0, 0.5. Comparisons with Ca_2FeMnO_5 and the Effect of the A-Site Cation. *Inorg. Chem.* **2011,** *50*, 7779-7791, doi.org/10.1021/ic200919m.
36. King, G.; Ramezanipour, F.; Llobet, A.; Greedan, J. E., Local structures of Sr_2FeMnO_{5+y} (y=0, 0.5) and $Sr_2Fe_{1.5}Cr_{0.5}O_5$ from reverse Monte Carlo modeling of pair distribution function data and implications for magnetic order. *J. Solid State Chem.* **2013,** *198*, 407-415, doi.org/10.1016/j.jssc.2012.11.005.
37. Ramezanipour, F.; Cowie, B.; Derakhshan, S.; Greedan, J. E.; Cranswick, L. M. D., Crystal and magnetic structures of the brownmillerite compound $Ca_2Fe_{1.039(8)}Mn_{0.962(8)}O_5$. *J. Solid State Chem.* **2009,** *182*, 153-159, doi.org/10.1016/j.jssc.2008.10.010.
38. Andreola, F.; Leonelli, C.; Romagnoli, M.; Miselli, P., Techniques Used to Determine Porosity. *Am. Cer. Soc. Bull.* **2000,** *79*, 49-52.

39. Lu, C.-H.; Bai, J.-H.; Chen, H., Preparation, sintering, and microstructures of strontium barium bismuth tantalate layered perovskite ceramics. *J. Mater. Sci.* **2004,** *39*, 3079-3083, doi.org/10.1023/B:JMSC.0000025835.22825.5c.
40. Choi, S.; Park, Y.; Yang, H.; Jin, H.; Tomboc, G. M.; Lee, K., Vacancy-engineered catalysts for water electrolysis. *CrystEngComm* **2020,** *22*, 1500-1513, doi.org/10.1039/C9CE01883B.
41. Sun, H.; Xu, X.; Hu, Z.; Tjeng, L. H.; Zhao, J.; Zhang, Q.; Lin, H.-J.; Chen, C.-T.; Chan, T.-S.; Zhou, W.; Shao, Z., Boosting the oxygen evolution reaction activity of a perovskite through introducing multi-element synergy and building an ordered structure. *J. Mater. Chem. A* **2019,** *7*, 9924-9932, doi.org/10.1039/C9TA01404G.
42. Benson, J.; Li, M.; Wang, S.; Wang, P.; Papakonstantinou, P., Electrocatalytic Hydrogen Evolution Reaction on Edges of a Few Layer Molybdenum Disulfide Nanodots. *ACS Appl. Mater. Interfaces* **2015,** *7*, 14113-14122, doi.org/10.1021/acsami.5b03399.
43. Yang, X.; Zhao, Z.; Yu, X.; Feng, L., Electrochemical hydrogen evolution reaction boosted by constructing Ru nanoparticles assembled as a shell over semimetal Te nanorod surfaces in acid electrolyte. *Chem. Commun.* **2019,** *55*, 1490-1493, doi.org/10.1039/C8CC09993F.
44. He, J.; Song, L.; Yan, J.; Kang, N.; Zhang, Y.; Wang, W., Hydrogen Evolution Reaction Property in Alkaline Solution of Molybdenum Disulfide Modified by Surface Anchor of Nickel–Phosphorus Coating. *Metals* **2017,** *7*, 211, doi.org/10.3390/met7060211.
45. Galal, A.; Atta, N. F.; Ali, S. M., Investigation of the catalytic activity of $LaBO_3$ (B=Ni, Co, Fe or Mn) prepared by the microwave-assisted method for hydrogen evolution in acidic medium. *Electrochim. Acta* **2011,** *56*, 5722-5730, doi.org/10.1016/j.electacta.2011.04.045.
46. Zhu, J.; Wang, Z.-C.; Dai, H.; Wang, Q.; Yang, R.; Yu, H.; Liao, M.; Zhang, J.; Chen, W.; Wei, Z.; Li, N.; Du, L.; Shi, D.; Wang, W.; Zhang, L.; Jiang, Y.; Zhang, G., Boundary activated hydrogen evolution reaction on monolayer MoS2. *Nat. Commun.* **2019,** *10*, 1348, doi.org/10.1038/s41467-019-09269-9.
47. Chai, L.; Yuan, W.; Cui, X.; Jiang, H.; Tang, J.; Guo, X., Surface engineering-modulated porous N-doped rod-like molybdenum phosphide catalysts: towards high activity and stability for hydrogen evolution reaction over a wide pH range. *RSC Adv.* **2018,** *8*, 26871-26879, doi.org/10.1039/C8RA03909G.
48. Hwang, B.-J.; Chen, H.-C.; Mai, F.-D.; Tsai, H.-Y.; Yang, C.-P.; Rick, J.; Liu, Y.-C., Innovative Strategy on Hydrogen Evolution Reaction Utilizing Activated Liquid Water. *Sci. Rep.* **2015,** *5*, 16263, DOI: 10.1038/srep16263.
49. Mohammed-Ibrahim, J.; Sun, X., Recent progress on earth abundant electrocatalysts for hydrogen evolution reaction (HER) in alkaline medium to achieve efficient water splitting – A review. *J. Energy Chem.* **2019,** *34*, 111-160, 10.1016/j.jechem.2018.09.016.
50. Sun, Q.; Dai, Z.; Zhang, Z.; Chen, Z.; Lin, H.; Gao, Y.; Chen, D., Double perovskite $PrBaCo_2O_{5.5}$: An efficient and stable electrocatalyst for hydrogen evolution reaction. *J. Power Sources* **2019,** *427*, 194-200, doi.org/10.1016/j.jpowsour.2019.04.070.
51. Uosaki, K.; Elumalai, G.; Dinh, H. C.; Lyalin, A.; Taketsugu, T.; Noguchi, H., Highly Efficient Electrochemical Hydrogen Evolution Reaction at Insulating Boron Nitride Nanosheet on Inert Gold Substrate. *Sci. Rep.* **2016,** *6*, 32217, doi.org/10.1038/srep32217.
52. Li, Y. H.; Liu, P. F.; Pan, L. F.; Wang, H. F.; Yang, Z. Z.; Zheng, L. R.; Hu, P.; Zhao, H. J.; Gu, L.; Yang, H. G., Local atomic structure modulations activate metal oxide as electrocatalyst for hydrogen evolution in acidic water. *Nat. Commun.* **2015,** *6*, 8064, doi.org/10.1038/ncomms9064.
53. Guo, X.; Tong, X.; Wang, Y.; Chen, C.; Jin, G.; Guo, X.-Y., High photoelectrocatalytic performance of a MoS_2–SiC hybrid structure for hydrogen evolution reaction. *J. Mater. Chem. A* **2013,** *1*, 4657-4661, doi.org/10.1039/C3TA10600D.

54. Song, X.; Chen, G.; Guan, L.; Zhang, H.; Tao, J., Interfacial engineering of MoS_2/TiO_2hybrids for enhanced electrocatalytic hydrogen evolution reaction. *Appl. Phys. Express* **2016,** *9*, 095801, 10.7567/APEX.9.095801.
55. Li, A.; Sun, Y.; Yao, T.; Han, H., Earth-Abundant Transition-Metal-Based Electrocatalysts for Water Electrolysis to Produce Renewable Hydrogen. *Chem.: Eur. J.* **2018,** *24*, 18334-18355, doi.org/10.1002/chem.201803749.
56. Chaitoglou, S.; Giannakopoulou, T.; Speliotis, T.; Vavouliotis, A.; Trapalis, C.; Dimoulas, A., Mo_2C/graphene heterostructures: low temperature chemical vapor deposition on liquid bimetallic Sn–Cu and hydrogen evolution reaction electrocatalytic properties. *Nanotechnology* **2019,** *30*, 125401, DOI: 10.1088/1361-6528/aaf9e8.
57. Zhang, X.; Zhang, M.; Tian, Y.; You, J.; Yang, C.; Su, J.; Li, Y.; Gao, Y.; Gu, H., In situ synthesis of MoS_2/graphene nanosheets as free-standing and flexible electrode paper for high-efficiency hydrogen evolution reaction. *RSC Adv.* **2018,** *8*, 10698-10705, doi.org/10.1039/C8RA01226A.
58. Lai, B.; Singh, S. C.; Bindra, J. K.; Saraj, C. S.; Shukla, A.; Yadav, T. P.; Wu, W.; McGill, S. A.; Dalal, N. S.; Srivastava, A.; Guo, C., Hydrogen evolution reaction from bare and surface-functionalized few-layered MoS_2 nanosheets in acidic and alkaline electrolytes. *Mater. Today Chem.* **2019,** *14*, 100207, doi.org/10.1016/j.mtchem.2019.100207.
59. Xi, W.; Yan, G.; Tan, H.; Xiao, L.; Cheng, S.; Khan, S. U.; Wang, Y.; Li, Y., Superaerophobic P-doped $Ni(OH)_2/NiMoO_4$ hierarchical nanosheet arrays grown on Ni foam for electrocatalytic overall water splitting. *Dalton Trans.* **2018,** *47*, 8787-8793, DOI: 10.1039/c8dt00765a.
60. Liu, M.-R.; Hong, Q.-L.; Li, Q.-H.; Du, Y.; Zhang, H.-X.; Chen, S.; Zhou, T.; Zhang, J., Cobalt Boron Imidazolate Framework Derived Cobalt Nanoparticles Encapsulated in B/N Codoped Nanocarbon as Efficient Bifunctional Electrocatalysts for Overall Water Splitting. *Adv. Func. Mater.* **2018,** *28*, 1801136, doi.org/10.1002/adfm.201801136.
61. Tavakkoli, M.; Kallio, T.; Reynaud, O.; Nasibulin, A. G.; Sainio, J.; Jiang, H.; Kauppinen, E. I.; Laasonen, K., Maghemite nanoparticles decorated on carbon nanotubes as efficient electrocatalysts for the oxygen evolution reaction. *J. Mater. Chem. A* **2016,** *4*, 5216-5222, doi.org/10.1039/C6TA01472K.
62. Pan, Y.; Chen, Y.; Li, X.; Liu, Y.; Liu, C., Nanostructured nickel sulfides: phase evolution, characterization and electrocatalytic properties for the hydrogen evolution reaction. *RSC Adv.* **2015,** *5*, 104740-104749, doi.org/10.1039/C5RA18737K.
63. Lv, X.; Zhu, Y.; Jiang, H.; Yang, X.; Liu, Y.; Su, Y.; Huang, J.; Yao, Y.; Li, C., Hollow mesoporous $NiCo_2O_4$ nanocages as efficient electrocatalysts for oxygen evolution reaction. *Dalton Trans.* **2015,** *44*, 4148-4154, doi.org/10.1039/C4DT03803G.
64. Oh, S.; Kim, H.; Kwon, Y.; Kim, M.; Cho, E.; Kwon, H., Porous Co–P foam as an efficient bifunctional electrocatalyst for hydrogen and oxygen evolution reactions. *J. Mater.Chem. A* **2016,** *4*, 18272-18277, doi.org/10.1039/C6TA06761A.
65. Song, F.; Hu, X., Ultrathin cobalt–manganese layered double hydroxide Is an efficient oxygen evolution catalyst. *J. Am. Chem. Soc.* **2014,** *136*, 16481-16484, doi.org/10.1021/ja5096733.
66. Moir, J.; Soheilnia, N.; O'Brien, P.; Jelle, A.; Grozea, C. M.; Faulkner, D.; Helander, M. G.; Ozin, G. A., Enhanced hematite water electrolysis using a 3D antimony-doped tin oxide electrode. *ACS Nano* **2013,** *7*, 4261-4274, doi.org/10.1021/nn400744d.
67. He, D.; He, G.; Jiang, H.; Chen, Z.; Huang, M., Enhanced durability and activity of the perovskite electrocatalyst $Pr_{0.5}Ba_{0.5}CoO_{3-\delta}$ by Ca doping for the oxygen evolution reaction at room temperature. *Chem. Commun.* **2017,** *53*, 5132-5135, doi.org/10.1039/C7CC00786H.
68. Shaula, A. L.; Kharton, V. V.; Patrakeev, M. V.; Waerenborgh, J. C.; Rojas, D. P.; Marques, F. M. B., Defect formation and transport in $SrFe_{1-x}Al_xO_{3-\delta}$. *Ionics* **2004,** *10*, 378-384, doi.org/10.1007/BF02377997.

69. Patrakeev, M. V.; Kharton, V. V.; Bakhteeva, Y. A.; Shaula, A. L.; Leonidov, I. A.; Kozhevnikov, V. L.; Naumovich, E. N.; Yaremchenko, A. A.; Marques, F. M. B., Oxygen nonstoichiometry and mixed conductivity of $SrFe_{1-x}M_xO_{3-\delta}$ (M=Al, Ga): Effects of B-site doping. *Solid State Sci.* **2006,** *8*, 476-487, doi.org/10.1016/j.solidstatesciences.2006.01.006.
70. Asenath-Smith, E.; Misture, S. T.; Edwards, D. D., Structural behavior and thermoelectric properties of the brownmillerite system $Ca_2(ZnxFe_{2-x})O_5$. *J. Solid State Chem.* **2011,** *184*, 2167-2177, doi.org/10.1016/j.jssc.2011.06.009.
71. Pommier, A.; Leinenweber, K. D., Electrical cell assembly for reproducible conductivity experiments in the multi-anvil. *Am. Mineral.* **2018,** *103*, 1298–1305, doi.org/10.2138/am-2018-6448.
72. Achary, P. G. R.; Munisha, B.; Singh, D. S.; Parida, K. S., Study of Electrical Properties of Nickel Doped Polyurethane Nanocomposites. *Polym. Sci.* **2018,** *4*, No.1:7, 10.4172/2471-9935.100035.
73. Singh, Y., Electrical Resistivity Measurements: a Review. *Int. J. Modern Phys.: Conference Series* **2013,** *22*, 745–756, doi.org/10.1142/S2010194513010970.
74. Tao; Canales-Vázquez, J.; Irvine, J. T. S., Structural and Electrical Properties of the Perovskite Oxide Sr_2FeNbO_6. *Chem. Mater.* **2004,** *16*, 2309-2316, doi.org/10.1021/cm049923+.
75. Zhang, Q.; Xu, Z. F.; Wang, L. F.; Gao, S. H.; Yuan, S. J., Structural and electromagnetic properties driven by oxygen vacancy in $Sr_2FeMoO_{6-\delta}$ double perovskite. *J. Alloys Compd.* **2015,** *649*, 1151-1155, doi.org/10.1016/j.jallcom.2015.07.211.
76. Mineshige, A.; Inaba, M.; Yao, T.; Ogumi, Z.; Kikuchi, K.; Kawase, M., Crystal Structure and Metal–Insulator Transition of $La_{1-x}Sr_xCoO_3$. *J.Solid State Chem.* **1996,** *121*, 423-429, doi.org/10.1006/jssc.1996.0058.
77. Mineshige, A.; Kobune, M.; Fujii, S.; Ogumi, Z.; Inaba, M.; Yao, T.; Kikuchi, K., Metal–Insulator Transition and Crystal Structure of $La_{1-x}Sr_xCoO_3$as Functions of Sr-Content, Temperature, and Oxygen Partial Pressure. *J. Solid State Chem.* **1999,** *142*, 374-381, doi.org/10.1006/jssc.1998.8051.
78. Cheng, X.; Fabbri, E.; Nachtegaal, M.; Castelli, I. E.; El Kazzi, M.; Haumont, R.; Marzari, N.; Schmidt, T. J., Oxygen evolution reaction on $La_{1-x}Sr_xCoO_3$ perovskites: a combined experimental and theoretical study of their structural, electronic, and electrochemical properties. *Chem. Mater.* **2015,** *27*, 7662-7672, doi.org/10.1021/acs.chemmater.5b03138.
79. Pizzini, S., Physical chemistry of semiconductor materials and processes *John Wiley & Sons Ltd, West Sussex, United Kingdom* **2015**.
80. Asenath-Smith, E.; Lokuhewa, I. N.; Misture, S. T.; Edwards, D. D., p-Type thermoelectric properties of the oxygen-deficient perovskite $Ca_2Fe_2O_5$ in the brownmillerite structure. *J. Solid State Chem.* **2010,** *183*, 1670-1677, doi.org/10.1016/j.jssc.2010.05.016.
81. Andoulsi, R.; Horchani-Naifer, K.; Férid, M., Electrical conductivity of $La_{1-x}Ca_xFeO_{3-\delta}$ solid solutions. *Ceram. Int.* **2013,** *39*, 6527-6531, doi.org/10.1016/j.ceramint.2013.01.085.
82. Jain, S. D.; Sahasrabudhe, G. G., *Engineering physics*. 1 ed.; Universities Press: *2010*, p-365.
83. Kim, Y. T.; Lopes, P. P.; Park, S. A.; Lee, A. Y.; Lim, J.; Lee, H.; Back, S.; Jung, Y.; Danilovic, N.; Stamenkovic, V.; Erlebacher, J.; Snyder, J.; Markovic, N. M., Balancing activity, stability and conductivity of nanoporous core-shell iridium/iridium oxide oxygen evolution catalysts. *Nat. Commun.* **2017,** *8*, 1449, doi.org/10.1038/s41467-017-01734-7.
84. Pramana, S. S.; Cavallaro, A.; Li, C.; Handoko, A. D.; Chan, K. W.; Walker, R. J.; Regoutz, A.; Herrin, J. S.; Yeo, B. S.; Payne, D. J.; Kilner, J. A.; Ryan, M. P.; Skinner, S. J., Crystal structure and surface characteristics of Sr-doped $GdBaCo_2O_{6-\delta}$ double perovskites: oxygen evolution reaction and conductivity. *J. Mater. Chem. A* **2018,** *6*, 5335-5345, doi.org/10.1039/C7TA06817D.

85. Lee, D. G.; Gwon, O.; Park, H. S.; Kim, S. H.; Yang, J.; Kwak, S. K.; Kim, G.; Song, H. K., Conductivity-dependent completion of oxygen reduction on oxide catalysts. *Angew. Chem., Int. Ed.* **2015,** *54*, 15730–15733, doi.org/10.1002/ange.201508129.
86. Zou, S.; Burke, M. S.; Kast, M. G.; Fan, J.; Danilovic, N.; Boettcher, S. W., Fe (Oxy)hydroxide Oxygen Evolution Reaction Electrocatalysis: Intrinsic Activity and the Roles of Electrical Conductivity, Substrate, and Dissolution. *Chem. Mater.* **2015,** *27*, 8011-8020, doi.org/10.1021/acs.chemmater.5b03404.
87. Viswanathan, V.; Pickrahn, K. L.; Luntz, A. C.; Bent, S. F.; Nørskov, J. K., Nanoscale Limitations in Metal Oxide Electrocatalysts for Oxygen Evolution. *Nano Lett.* **2014,** *14*, 5853-5857, doi.org/10.1021/nl502775u.

For Table of Contents Use Only

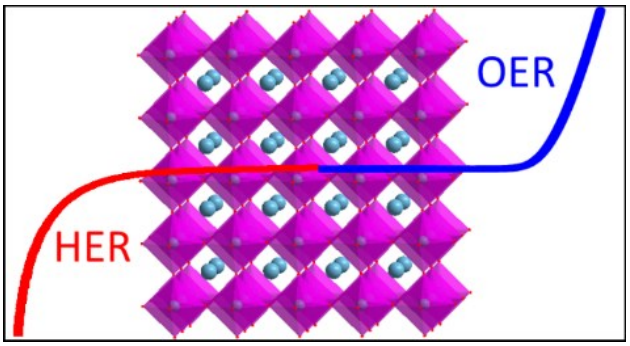

Synopsis:
A highly active water-splitting electrocatalyst based on earth-abundant metals is discovered, which is an important development in sustainable chemistry.